1 E06-014

A Precision Measurement of d_2^n: Probing the Lorentz Color Force

S. Choi, X. Jiang, Z.-E. Meziani, B. Sawatzky, spokespersons,
and
the d_2^n and Hall A Collaborations.
Contributed by D. Flay, D. Parno and M. Posik.

1.1 Physics Motivation

1.1.1 d_2^n: Quark-Gluon Correlations in the Nucleon

To date, extensive work has been done investigating the spin structure function g_1 within the context of the Feynman parton model and pQCD. However, far less is known about the g_2 structure function. It is known to contain quark-gluon correlations. It follows from a spin-flip Compton amplitude and may be written as:

$$g_2\left(x,Q^2\right) = g_2^{WW}\left(x,Q^2\right) + \bar{g}_2\left(x,Q^2\right), \tag{1}$$

where g_2^{WW} is the Wandzura-Wilczek term, which may be expressed entirely in terms of g_1 [1]:

$$g_2^{WW}\left(x,Q^2\right) = -g_1\left(x,Q^2\right) + \int_x^1 \frac{g_1\left(y,Q^2\right)}{y} dy. \tag{2}$$

The second term is given as:

$$\bar{g}_2\left(x,Q^2\right) = -\int_x^1 \frac{1}{y}\frac{\partial}{\partial y}\left[\frac{m_q}{M} h_T\left(y,Q^2\right) + \xi\left(y,Q^2\right)\right] dy, \tag{3}$$

where h_T is the transverse polarization density, and ξ is a term arising from quark-gluon correlations. Here, h_T is suppressed by the ratio of the quark mass m_q to the target mass M. Therefore, a measurement of $\bar{g}_2$ provides access to quark-gluon interactions inside the nucleon [2].

Additionally, a measurement of both g_1 and g_2 allows for the determination of the quantity d_2^n, which is formed as the second moment of a linear combination of g_1 and g_2:

$$d_2^n\left(Q^2\right) = \int_0^1 x^2\left[2g_1\left(x,Q^2\right) + 3g_2\left(x,Q^2\right)\right] dx = 3\int_0^1 x^2 \bar{g}_2\left(x,Q^2\right) dx. \tag{4}$$

d_2^n also appears as a matrix element of a twist-3 operator in the operator product expansion [3]:

$$\langle P,S \mid \bar{\psi}_q(0)\, gG^{+y}(0)\,\gamma^+ \psi_q(0) \mid P,S\rangle = 2MP^+P^+S^x d_2^n, \tag{5}$$

where $G^{+y} = \frac{1}{\sqrt{2}}\left(B^x - E^y\right)$. We see from Equations 3–5 that d_2^n is a twist-3 matrix element that measures quark-gluon interactions.

Recent work has shown [4, 5] that at high Q^2, d_2^n is seen as a color Lorentz force averaged over the volume of the nucleon. This is given by the expression of the transverse (color) force on the active quark immediately following its interaction with a virtual photon:

$$F^y(0) \equiv -\frac{\sqrt{2}}{2P^+}\langle P,S \mid \bar{\psi}_q(0)\, gG^{+y}(0)\,\gamma^+ \psi_q(0) \mid P,S\rangle = -\frac{1}{2}M^2 d_2^n. \tag{6}$$

This theoretical interpretation reveals how g_2 and subsequently d_2^n will allow us to examine the color interactions of the constituents inside the nucleon.

While bag and soliton model calculations of d_2 for the neutron yield numerical values consistent with those of lattice QCD, current experimental data differs by roughly two standard deviations (see the highest Q^2 data in Figure 1). One of the goals of our experiment is to improve the experimental error on the value of d_2^n by a factor of four. It subsequently provides a benchmark test of lattice QCD calculations, shown in Figure 1.

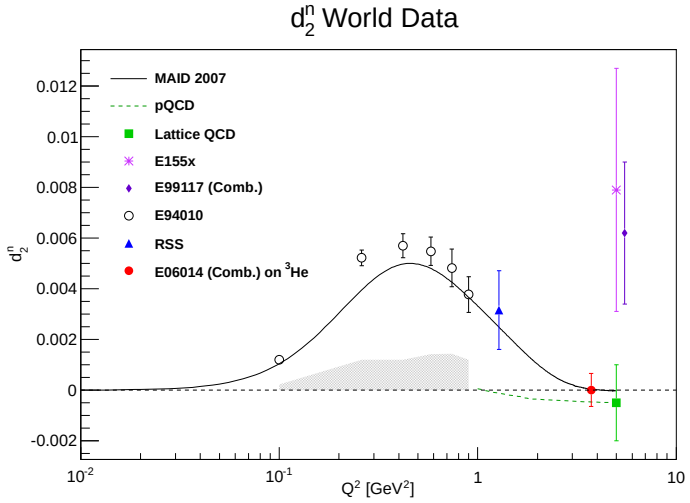

Figure 1: d_2^n as a function of Q^2. All the data shown with the exception of the SLAC E155x data are dominated by resonance contributions. E06-014 data will observe mostly the deep inelastic scattering (DIS) contribution. The projected error on from E06-014 [6] is shown, along with the lattice QCD result [7]. The dashed green curve shows the pQCD evolution from the lattice point [8] based on the calculations of [9, 10]. Data from JLab experiments E94-010 [11] and RSS [12] are included in the plot. For comparison to the resonance contribution, a MAID model [13] is plotted. Also plotted is the total d_2 from SLAC experiment E155x [14].

1.1.2 A_1: The Virtual Photon-Nucleon Asymmetry

Another quantity of interest is the virtual photon-nucleon longitudinal spin asymmetry A_1. It provides insight into the quark structure of the nucleon and can be defined as:

$$A_1\left(x,Q^2\right) \equiv \frac{\sigma_{1/2}-\sigma_{3/2}}{\sigma_{1/2}+\sigma_{3/2}}, \tag{7}$$

where the subscript 1/2 (3/2) gives the projection of the total spin of the virtual photon-nucleon system along the virtual photon direction corresponding to the nucleon's spin anti-parallel (parallel) to the virtual photon. Constituent quark models (CQM) and pQCD models predict A_1 to be large and positive at large x. Figure 2(a) shows the current world data compared to these models. It is seen that the CQM (yellow band [15]) describes the trend of the data reasonbly well. The pQCD parameterization with hadron helicity conservation (dark blue curve [20])—assuming quark orbital angular momentum to be zero—does not describe the data well. However, the pQCD model allowing for quark orbital angular momentum to be non-zero (green curve [21]) describes the data well, pointing perhaps to the importance of quark orbital angular momentum in the spin structure of the nucleon.

Combining A_1^n data measured on a polarized effective neutron target with A_1^p data measured on a polarized proton target allows access to $\Delta u/u$ and $\Delta d/d$. Recent results from Hall A [19] and from CLAS [22] showed a signicant deviation of $\Delta d/d$ from the pQCD predictions, which have that ratio approaching 1 in the limit of $x \to 1$ (Fig. 2(b)). As part of the 12 GeV program, two approved experiments (one in Hall A [23] and one in Hall C [24]) will extend the accuracy and x range of this measurement, but a measurement of A_1^n at the kinematics of this experiment (E06-014) will provide valuable support (or refutation) of prior JLab results, while producing additional input for theoretical models in advance of the coming experiments at 12 GeV.

1.2 The Experiment

The experiment ran in Hall A of Jefferson Lab from February to March of 2009, with two beam energies of $E = 4.73$ and 5.89 GeV, covering the resonance and deep inelastic valence quark regions, characterized by $0.2 \leq x \leq 0.7$ and $2\ \text{GeV}^2 \leq Q^2 \leq 6\ \text{GeV}^2$. The coverage in the x and Q^2 plane is shown in Figure 3.

In order to calculate d_2^n, we scattered a longitudinally polarized electron beam off of a ^{3}He target, in two polarization configurations – longitudinal and transverse. ^{3}He serves as an effective polarized neutron target since roughly

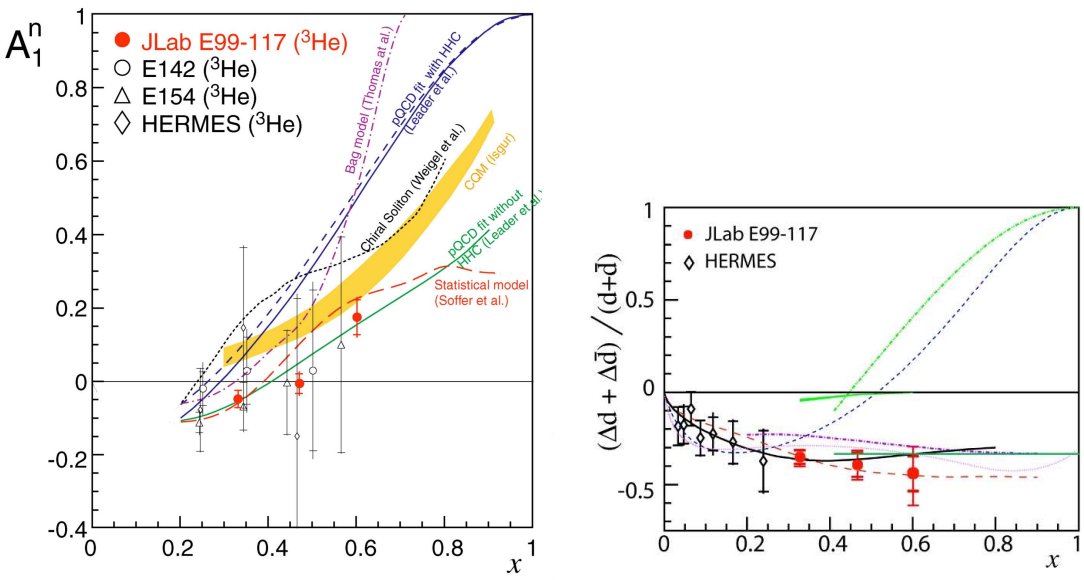

(a) A_1^n (b) $\Delta d/d$

Figure 2: Current data for A_1^n and $\Delta d/d$. (a): The current world data for the neutron A_1 from SLAC E143 [16] and E154 [17] and HERMES [18], along with JLab E99-117 [19]. Also shown are CQM models and various pQCD models; (b): the corresponding models and data from HERMES and JLab for $\Delta d/d$.

86% of the polarization is carried by the neutron. This is due to the two protons in the nucleus being primarily bound in a spin singlet state [25, 26].

We measured the unpolarized total cross section σ_0 and the asymmetries $A_\parallel$ and $A_\perp$. The cross section was measured by the Left High-Resolution Spectrometer (LHRS), while the asymmetries were measured by the BigBite Spectrometer. The LHRS and BigBite were oriented at scattering angles of $\theta = 45^\circ$ to the left and right of the beamline, respectively.

Expressing the structure functions entirely in terms of these experimental quantities, we have the expression for d_2^n:

$$d_2^n = \int_0^1 \frac{MQ^2}{4\alpha^2} \frac{x^2y^2}{(1-y)(2-y)} \sigma_0 \left[\left(3\frac{1+(1-y)\cos\theta}{(1-y)\sin\theta} + \frac{4}{y}\tan(\theta/2) \right) A_\perp + \left(\frac{4}{y} - 3 \right) A_\parallel \right] dx, \tag{8}$$

where $x = Q^2/2M\nu$, $\nu = E - E'$ is the energy transfer to the target, E' is the scattered electron energy, and $y = \nu/E$ is the fractional energy transfer to the target. The asymmetries are given by:

$$A_\parallel = \frac{N^{\downarrow\Uparrow} - N^{\uparrow\Uparrow}}{N^{\downarrow\Uparrow} + N^{\uparrow\Uparrow}} \quad \text{and} \quad A_\perp = \frac{N^{\downarrow\Rightarrow} - N^{\uparrow\Rightarrow}}{N^{\downarrow\Rightarrow} + N^{\uparrow\Rightarrow}},$$

where N is the number of electron counts measured for a given configuration of beam helicity (single arrows) and target spin direction (double-arrows).

While d_2^n was the main focus of the experiment, the measurement of the asymmetries allowed for the extraction of A_1^n, according to:

$$A_1^n = \frac{1}{D(1+\eta\xi)} A_\parallel^n - \frac{\eta}{d(1+\eta\xi)} A_\perp^n, \tag{9}$$

where D, η, ξ and d are kinematic factors [27].

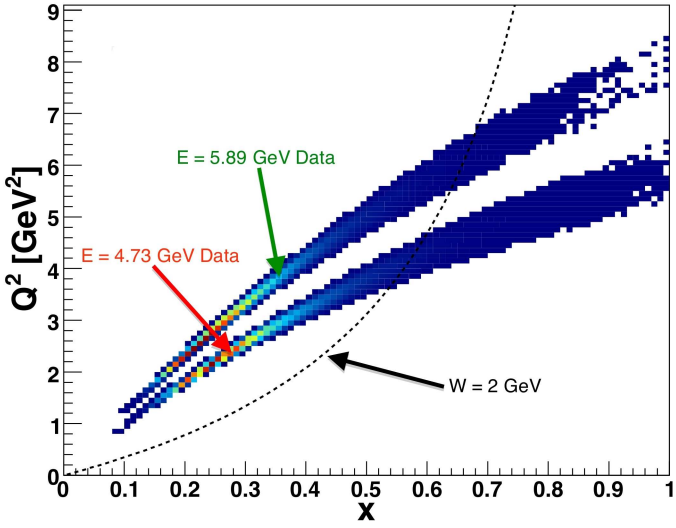

Figure 3: The E06-014 kinematic coverage in Q^2 and x. The lower band is the 4.73 GeV data set and the upper band is the 5.89 GeV data set. The black dashed line shows W = 2 GeV. The data to the left and right of this line corresponds to DIS and resonance data, respectively.

1.3 Beam Polarization

E06-014 used a polarized electron beam at energies of 4.73 and 5.89 GeV. The polarization of the electron beam was measured independently through Compton and Møller scattering. During the running of E06-014, there were several Møller measurements performed while Compton measurements were taken continuously throughout the experiment. Figure 4 shows the beam polarization as a function of BigBite run number for the Møller and Compton results. The beam polarization data was split into four run sets and the average polarization for each run period was then computed by taking into account both the Compton and Møller data. The final beam polarizations can be seen in Table 1 [28].

Run Set	Beam Energy (GeV)	P_e from Compton	P_e from Møller	Combined P_e
1	5.90	0.726 ± 0.018	0.745 ± 0.015	0.737 ± 0.012
2	4.74	0.210 ± 0.011	-	0.210 ± 0.011
3	5.90	0.787 ± 0.020	0.797 ± 0.016	0.793 ± 0.012
4	4.74	0.623 ± 0.016	0.628 ± 0.012	0.626 ± 0.010

Table 1: Final beam polarization for E06-014, corrected for beam fluctuations. For run set 2 there was no Møller measurement. [28]

1.4 ^{3}He Target Density

A complete understanding of the target density is essential, since the calculation of the target polarization from the EPR and NMR measurements depends on the ^{3}He density. The number density of ^{3}He was measured in both the pumping and the target chambers. This measurement was achieved by exploiting the fact that collisions with ^{3}He atoms broaden the D1 and D2 absorption lines of rubidium [29]. The ^{3}He number density at room temperature, n_0, can be obtained by measuring the width of the D1 and D2 absorption lines and subtracting a 1% N_2 contribution.

The full analysis to determine the ^{3}He density may be found in [31].

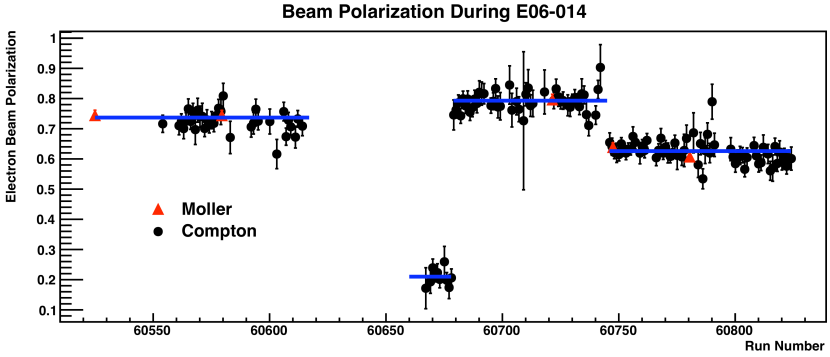

Figure 4: Final electron beam polarization from Møller and Compton measurements for E06-014. Note there was no Møller measurement for the second run set [28].

1.5 Polarized ^{3}He Target

Knowledge of the target polarization is crucial when performing a double-spin asymmetry experiment. E06-014 used the standard Hall A polarized ^{3}He target with two holding field directions: longitudinal and transverse in plane, with respect to the electron beam direction. The target polarization was extracted through electron paramagnetic resonance (EPR). The longitudinal polarization was cross checked using nuclear magnetic resonance (NMR) measurements. EPR measurements were taken every several days during the experiment, while NMR measurements were taken every few hours.

1.5.1 EPR Calibration

The frequency shift of potassium level transitions in the presence of ^{3}He was measured using EPR. This frequency shift $\Delta\nu_{EPR}$ can be related to the target polarization, $P_{^3\mathrm{He}}$:

$$\Delta\nu_{EPR} = \frac{4\mu_0}{3}\frac{d\nu_{EPR}}{dB}\kappa_0\mu_{^3\mathrm{He}}n_{pc}P_{^3\mathrm{He}}, \tag{10}$$

where μ_0 is the vacuum permeability; $\mu_{^3\mathrm{He}}$ is the magnetic moment; $\frac{d\nu_{EPR}}{dB}$ is the derivative of the EPR frequency with respect to the magnetic field; κ_0 is the enhancement factor, and n_{pc} is the pumping chamber number density. EPR measurements give the absolute ^{3}He polarization in the pumping chamber. However, it is the ^{3}He polarization in the target cell that needs to be extracted. A polarization gradient model is used in order to determine the polarization between the two chambers. The change in polarization in the two chambers is given by:

$$\frac{dP_T}{dt} = d_P\left(P_T - P_P\right) + \gamma_{SE}\left(P_{Rb} - P_P\right) - \Gamma_P P_P \tag{11}$$

$$\frac{dP_P}{dt} = d_T\left(P_P - P_T\right) + \Gamma_T P_T, \tag{12}$$

where $P_{T,P,Rb}$ is the polarization of the target chamber, pumping chamber ^{3}He and rubidium atoms. Γ_T is the depolarization rate of the ^{3}He; γ_{SE} is the spin exchange rate between ^{3}He and rubidium atoms, and $d_{P,T}$ are diffusion constants that depend on the target cell geometries and ^{3}He density. Taking the equilibrium solution, we obtain an expression that relates the polarizations between the two chambers:

$$P_T = \frac{1}{1+\frac{\Gamma_T}{d_T}}P_P. \tag{13}$$

The calculated diffusion constant, d_T, is shown in Table 1.5.1 for both target spin directions. The depolarization rate is a sum of various depolarization rates caused by different sources as shown in Equation 14. $\Gamma^{He} + \Gamma^{wall}$ are determined by measuring the target cell polarization live time. The depolarization rate due to the beam, Γ^{beam}, was

Table 2: d_T diffusion constant for both target spin directions.

Parameter	Target Spin	Value	Units	Uncertainty [%]
d_T	Long.	0.892	hour^{-1}	15.04
d_T	Trans.	0.889	hour^{-1}	15.06

Table 3: List of parameters used to calculate Γ^T

Parameter	Value	Units	Uncertainty [%]
$\Gamma^{He}+\Gamma^{wall}$	0.0714	hour^{-1}	35
Γ^{beam}	0.0794	hour^{-1}	10.45
Γ^{AFP}	neg.	hour^{-1}	neg.
$\Gamma^{\nabla B}$	neg.	hour^{-1}	neg.
Γ_T	0.1508	h^{-1}	36.53

found by using a model [30]. $\Gamma^{\nabla B}$ was calculated by measuring the gradient magnetic holding fields which polarize the target, and were found to be negligible. Γ^{AFP} was also found to be negligible. Table 1.5.1 shows the results of the depolarization rates.

$$\Gamma_T = \Gamma^{He}+\Gamma^{wall}+\Gamma^{beam}+\Gamma^{AFP}+\Gamma^{\nabla B} \tag{14}$$

During EPR measurements, a NMR measurement was done simultaneously, allowing us to calibrate NMR measurements during production with the EPR measurements by taking the ratio of the target polarization measured by EPR, P_T, and the measured NMR amplitude, h. A conversion factor c' can then be formed that allows NMR measurements to be converted into an absolute ^{3}He polarization.

After applying the c' factor to all NMR measurements, a linear interpolation was done as a function of run time. This allowed the extraction of a target polarization on a run-by-run basis. The pumping and target chamber polarizations were extracted via EPR measurements, shown in Figure 5.

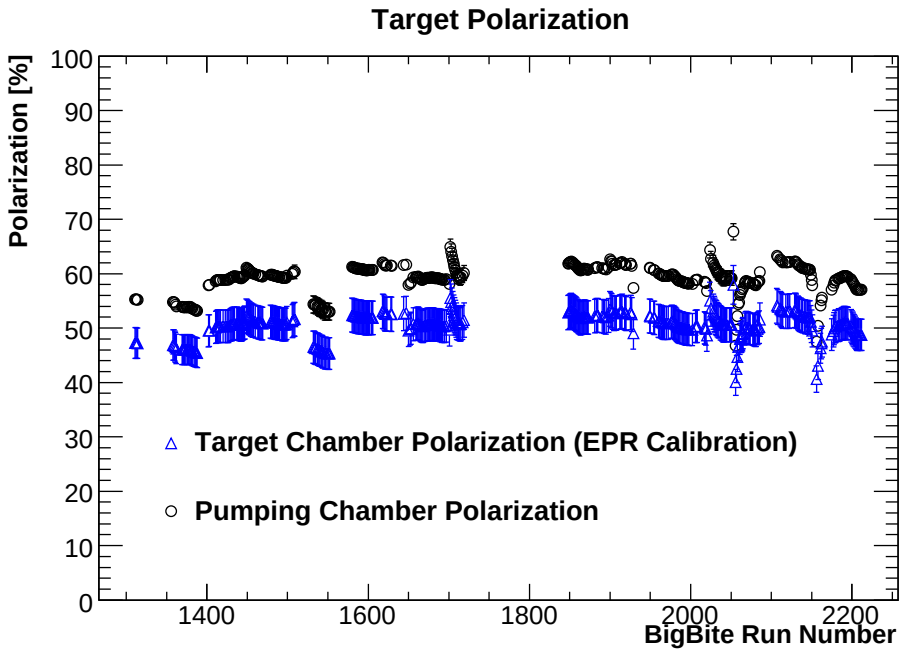

Figure 5: ^{3}He polarization in the pumping and target chambers. Some ^{3}He polarization is lost while traveling between the two chambers.

1.5.2 Water Calibration

In addition to calibrating the NMR using EPR measurements, NMR measurements on a water sample can also be used to calibrate ^{3}He NMR signals. The polarization of the protons in the water, when placed in a known magnetic field, can be solved exactly. The water polarization was measured by performing NMR measurements on a target cell filled with water. The water target cell was similar in geometry to the ^{3}He filled cells. The water NMR signal was detected in two sets of pick-up coils that extended the length of the target (40 cm) on both sides. A NMR cross-calibration factor needs to be applied when using the water calibration, because the NMR measurement for the water cell and ^{3}He target cell took place in two different locations and the signals were measured in two different pick-up coil sets. The cross-calibration factor can be calculated by selecting a ^{3}He target spin direction and then taking the ratio of the ^{3}He NMR signal measured in the pick-up coils at the water cell position and the ^{3}He NMR signal measured at the ^{3}He target cell position during a production run. This could in principle be done for all target spin directions, longitudinal and transverse. Unfortunately, there was no transverse NMR measurements with the ^{3}He in the water cell position; as a result, there is a large systematic uncertainty on the transverse target polarization. With this in mind, the water calibration for the longitudinal direction is used to cross-check the target polarization extracted from the longitudinal EPR calibration.

Due to the fact that the polarization of water is small ($\approx 7\times10^{-9}$), a water polarization model was used in order to fit the water NMR signal and accurately extract the NMR signal height. The time evolution of the water polarization can be described by the Bloch equations given as:

$$\frac{dP_x(t)}{dt} = -\frac{1}{T_2}P_x(t)+\gamma(H(t)-H_0)P_y(t)+\frac{1}{T_2}\chi H_1 \tag{15}$$

$$\frac{dP_y(t)}{dt} = -\gamma(H(t)-H_0)P_x(t)-\frac{1}{T_2}P_y(t)+\gamma H_1 P_z(t) \tag{16}$$

$$\frac{dP_z(t)}{dt} = -\gamma H_1 P_y(t)-\frac{1}{T_1}P_z(t)+\frac{1}{T_1}\chi H(t), \tag{17}$$

where P is the water polarization in a particular direction; t is the time; T_1 and T_2 are the longitudinal and transverse spin relaxation times; H_0 is the resonance field; H_1 is the transverse field component; $H(t)=H_0+\alpha t$ is the field component along the z-axis; $\alpha = 1.2$ G/s is the field sweep speed; γ is the gyro-magnetic ratio of the proton; $\chi=\frac{\mu_{p,H_2O}}{k_B T}$, with μ_{p,H_2O} being the magnetic moment of a proton in water; k_B is the Boltzmann constant and T is the target chamber temperature.

Using the Bloch equations, an effective polarization, $P_{eff}=\sqrt{P_x^2+P_y^2+P_z^2}$, can be calculated and leads to the integral equation shown in Equation 18. This equation was solved numerically using Mathematica. However, an analytic function is needed to fit the water NMR signal, so approximations to P_{eff} were made. Figure 6 shows the water NMR fit results for 6,189 NMR sweeps.

$$P_{eff}(t)=e^{-(t-t_i)/T_1}\left[P_{eq}(t_i)+\frac{1}{T_1}\int_{t_i}^{t}e^{(u-t_i)/T_1}P_{eq}(u)du\right] \tag{18}$$

While the geometries of the water and ^{3}He cells are similar, they are not identical. To correct for this discrepancy, the ratio of the magnetic flux through the ^{3}He and water cells was calculated. With this information, a water calibration constant can be formed, shown in Equation 19.

$$c_w=\left(\frac{P_w}{S_w}\right)\left(\frac{G_w}{G_{He}}\right)\left(\frac{\mu_p}{\mu_{He}}\right)\left(\frac{n_p\Phi_w}{n_{He}^{pc}\phi_{He}^{pc}+n_{He}^{tc}\phi_{He}^{tc}}\right)\left(\frac{S_{pick-up}^{He}}{S_{prod.}^{He}}\right), \tag{19}$$

where $w(p)$ means water target (proton), He means ^{3}He target, P is the polarization, S is the NMR signal height and μ is the magnetic moment. $S_{pick-up}$ is the NMR signal with the ^{3}He target measured at the pick-up coil location where the water NMR was done. $S_{prod.}$ is the NMR signal measured with the ^{3}He in the production position. Applying this constant to the interpolated NMR measurements, a run-by-run ^{3}He target polarization can be extracted. By comparing the longitudinal target polarizations extracted from the EPR and water calibrations, both methods were found to give consistent results.

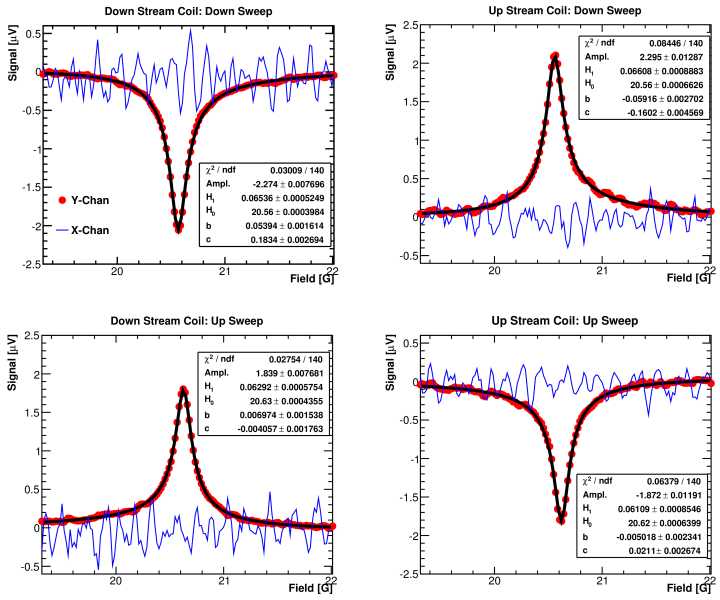

Figure 6: Presented are the sweep up and sweep down signals for the downstream and upstream coils. The Y lock-in channel is shown as red markers with water fit shown as a black line. The X lock-in channel is shown as a blue line.

1.6 The Left High-Resolution Spectrometer

1.6.1 Unpolarized Total Cross Sections

The Left High-Resolution Spectrometer (LHRS) was used to measure the unpolarized total cross section. The analysis for the extraction of the experimental cross section, σ_{rad}, for the E = 4.73 GeV and 5.89 GeV data sets is shown in [31].

1.6.2 Radiative Corrections

Electrons lose energy due to interactions with material. This includes the material before and after the target, and the target material itself. These interactions will alter the electron's *true* incident energy and also its *true* scattered energy. This ultimately results in a different cross section than the true value. These effects are characterized by ionization (or Landau straggling) and bremsstrahlung. There are also higher-order processes at the interaction vertex that must be considered. Collectively, the correction of these effects is called *radiative corrections*.

A first correction that must be done *before* carrying out the radiative corrections is to subtract the elastic radiative tail, since it affects all states of higher invariant mass W [32]. For these kinematics, the elastic tail is negligible and was not subtracted from the data.

The ^{3}He quasi-elastic tail, however, has a larger contribution and needs to be subtracted. The tail was built up from calculating the *elastic* tail of the proton and neutron using ROSETAIL [33] and adding them together as $2p+n$, to account for two protons and one neutron in ^{3}He. The systematic effect of the subtraction on the resulting cross section, σ_{rad}, was $\leq 0.5\%$.

In considering the effects mentioned above, the *measured* cross section is realized in terms of a triple-integral:

$$\sigma_{\text{rad}}\left(E_s,E_p\right) = \int_0^T \frac{dt}{T} \int_{E_s^{min}}^{E_s} dE_s' \int_{E_p}^{E_p^{max}} dE_p' I\left(E_s,E_s',t\right) \sigma_r\left(E_s',E_p'\right) I\left(E_p,E_p',T-t\right), \tag{20}$$

where σ_{rad} is the measured (radiated) cross section, σ_r is the *internally*-radiated cross section. E_s is the incident electron energy, E_p is the scattered electron energy. $I\left(E_0,E,t\right)$ is the probability of finding an electron with incident energy E_0 that has undergone bremsstrahlung with final energy E at a depth t inside a material [32, 34].

In order to *unfold* the Born cross section, an iterative procedure is carried out in RADCOR [35]. It amounts to an "energy-peaking" approximation, resulting in the calculation of:

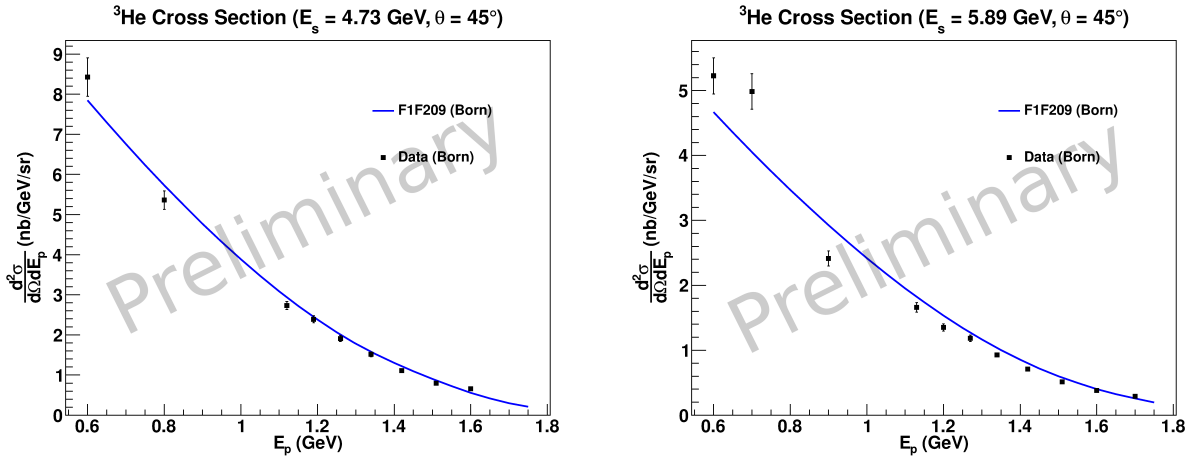

(a) E = 4.73 GeV

(b) E = 5.89 GeV

Figure 7: Unpolarized Born cross sections and P. Bosted's F1F209 model [36] as a function of scattered electron energy (E_p) for beam energies of 4.73 (a) and 5.89 GeV (b). The error bars are the in quadrature sum of statistical and systematic errors determined thus far (Sect. 1.6.3).

$$\sigma_b^i = \frac{1}{C}\left[\sigma_{\rm rad} - \int(\ldots)\,\sigma_b^{i-1}dE_s' - \int(\ldots)\,\sigma_b^{i-1}dE_p'\right], \tag{21}$$

where C and the two integrals are defined in Equation IV.2 in [32]. σ_b^i is the Born cross section obtained for the $i^{\rm th}$ iteration of the code, $\sigma_{\rm rad}$ is the radiated cross section to be corrected. σ_b^i is then re-inserted into equation for the next iteration. It was found that the calculation converges within the first 3–4 iterations. Figure 7 shows the Born cross sections.

In E06-014, we took data for only two E_s values of 4.73 GeV and 5.89 GeV. However, we need enough data to properly calculate the integrals above. Therefore, we used a suitable cross section model [36] to fill in the rest of the phase space for each data set.

1.6.3 Systematic Errors

Table 4 shows the systematic errors determined from the data as compared to the projected errors in the E06-014 proposal [6]. One large contribution comes from the cuts on the target variables; the cut on the horizontal scattering angle, ϕ, contributes at the $\sim$ 2% level. This is not surprising since the Mott cross section is most sensitive to this quantity. Another large contribution comes from the radiative corrections. The source of this is due to the dependence on the cross section model used and how accurately we know the material thicknesses in the electron's path before and after scattering. These two radiative correction errors combine for an error of $< 4\%$.

Type	Proposal (%)	Experiment (%)
PID Efficiency	≈ 1	1
Background Rejection Efficiency	≈ 1	1
Acceptance Cut	2–3	2.7
Target Density	2–3	2.2
Dead Time	< 1	< 1
Radiative Corrections	≤ 10	< 4

Table 4: The systematic errors on the Born cross section. The largest contributions come from the radiative corrections and the target cuts. However, all values are within the limits specified in the proposal.

1.7 The BigBite Spectrometer

1.7.1 The Double-Spin Asymmetries

The BigBite spectrometer was used to measure the parallel and perpendicular double-spin asymmetries between longitudinally polarized electrons and a longitudinally or transversely polarized ^{3}He target. These asymmetries were then corrected for imperfect beam and target polarizations. Corrections were also made for dilution effects due to the presence of N_2 in the target [29]. The full details of this analysis may be found in [31].

1.7.2 Positron Contamination Correction

In addition to N_2 contamination, pair-produced electrons can also contaminate the asymmetry. To remove this dilution, the *positron* asymmetry is measured on the BigBite spectrometer and is subtracted from the electron asymmetry as:

$$A_n^{e^-} = \frac{A_n^{\mathrm{raw},e^-} - RA_n^{e^+}}{1-R} \tag{22}$$

$$R = \frac{N_p^{e^+}}{N_n^{\mathrm{raw},e^-}}, \tag{23}$$

where $A_n^{e^-}$ is the corrected electron asymmetry; A_n^{raw,e^-} is the uncorrected electron asymmetry; $A_n^{e^+}$ is the positron asymmetry; R is the ratio of positron to electron events, serving as a weight factor to properly scale the positron asymmetry. The subscript n (p) refers to negative (positive) polarity. With BigBite in negative polarity, electrons bend up into the detector, whereas positrons bend downwards.

After applying this correction to the parallel and perpendicular asymmetries, we obtain the values shown in Figure 8(a) for E = 4.73 GeV and Figure 8(b) for E = 5.89 GeV. Radiative corrections have not been applied.

1.8 Preliminary Physics Results

In this section, we present our preliminary physics results for asymmetry $A_1^{^3\mathrm{He}}$and the spin structure functions g_1 and g_2 on ^{3}He. These results are preliminary because work is being done on the radiative corrections to the asymmetries along with a Geant4 simulation to further investigate the difference between the bend-up and bend-down acceptances in the BigBite spectrometer.

The extraction of $d_2^{^3\mathrm{He}}$ and $\mathrm{d_2^n}$ along with the neutron asymmetry A_1^n, and the spin structure functions $g_{1,2}$ are also underway; however, the extraction is model-dependent. Previous experiments [19] have used Bissey et al.'s complete model in the DIS regime [39]. However, E06-014's data spans both the DIS and resonance regions. A consistent treatment of both DIS and resonance data requires careful consideration of structure-function smearing [40]. We are working with W. Melnitchouk to extract neutron quantities across our entire kinematic range.

1.8.1 The Virtual Photon-Nucleon Asymmetry

Figure 9(a) and Figure 9(b) shows the preliminary result for $A_1^{^3\mathrm{He}}$ at E = 4.73 and 5.89 GeV, respectively. Also shown is world data from SLAC E142 [37] and JLab E01-012 [38] and E99-117 [19]. The red (blue) data points indicate the DIS (resonance) data for this experiment. No radiative corrections have been applied to these data. The data from this experiment are consistent with the world data across a wide range in x, despite the larger error bars in the resonance region.

1.8.2 The Spin Structure Functions

En route to extracting d_2^n, the spin structure functions g_1 and g_2 can be obtained according to:

$$g_1 = \frac{MQ^2}{4\alpha^2}\frac{2y}{(1-y)(2-y)}\sigma_0\left[A_\parallel + \tan(\theta/2)A_\perp\right] \tag{24}$$

$$g_2 = \frac{MQ^2}{4\alpha^2}\frac{y^2}{(1-y)(2-y)}\sigma_0\left[-A_\parallel + \frac{1+(1-y)\cos\theta}{(1-y)\sin\theta}A_\perp\right], \tag{25}$$

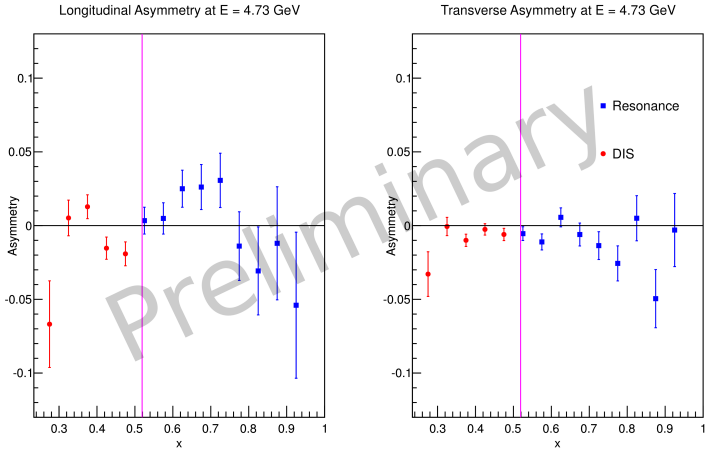

(a) E = 4.73 GeV

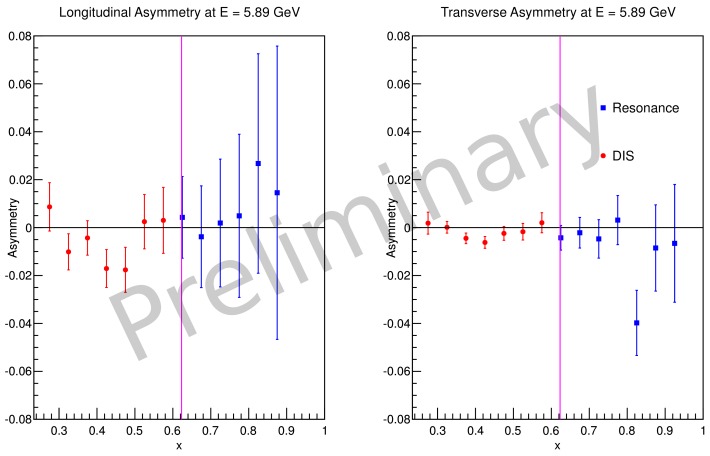

(b) E = 5.89 GeV

Figure 8: Physics asymmetries with positron corrections. The magenta line shows the DIS threshold, below which is the DIS region. No radiative corrections. (a): E = 4.73 GeV data; (b): E = 5.89 GeV data.

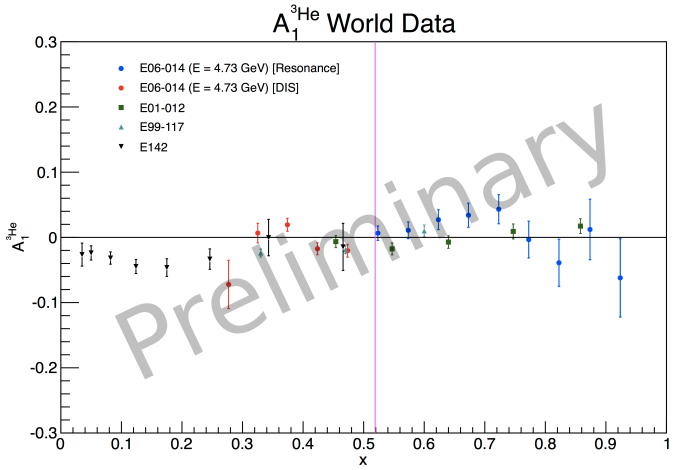

(a) E = 4.73 GeV

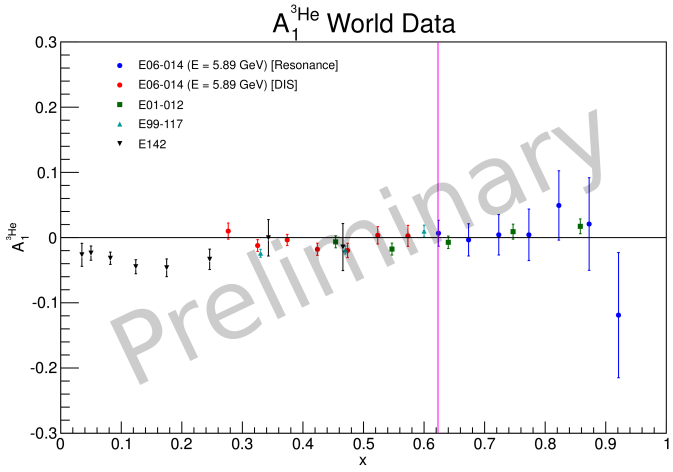

(b) E = 5.89 GeV

Figure 9: $A_1^{^3He}$ compared to the world data from SLAC E142 [37] and JLab E01-012 [38] and E99-117 [19]. (a): E = 4.73 GeV data; (b): E = 5.89 GeV data.

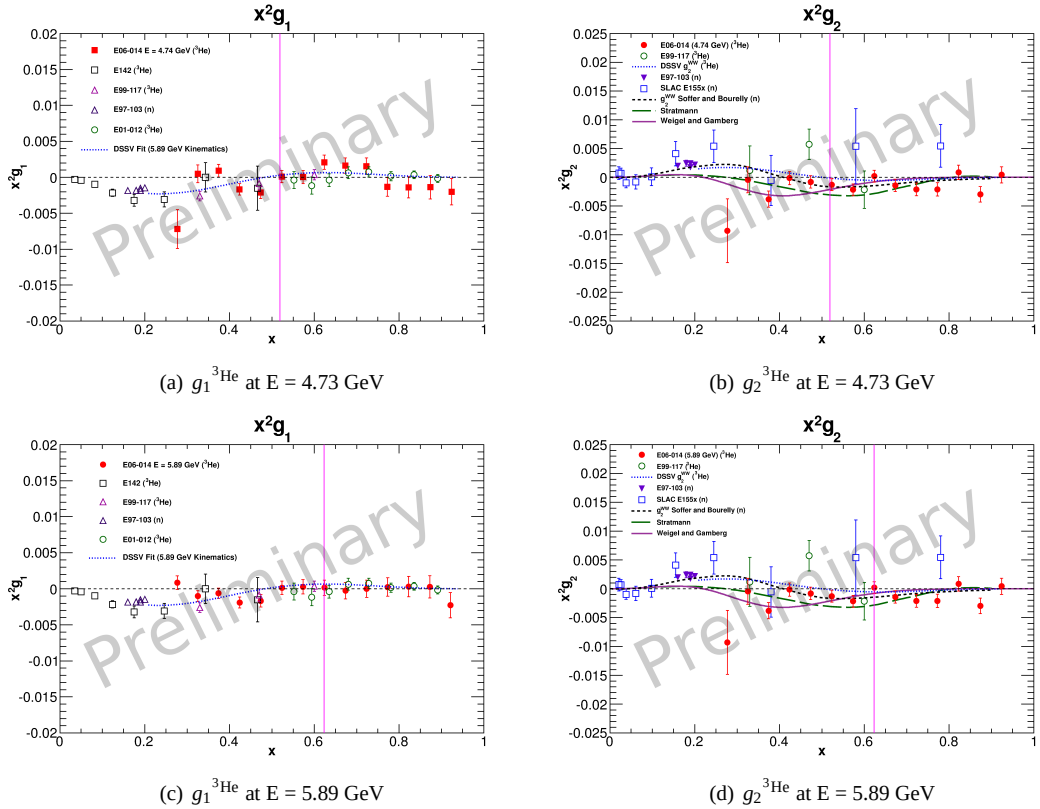

(a) $g_1{}^{3}\mathrm{He}$ at E = 4.73 GeV

(b) $g_2{}^{3}\mathrm{He}$ at E = 4.73 GeV

(c) $g_1{}^{3}\mathrm{He}$ at E = 5.89 GeV

(d) $g_2{}^{3}\mathrm{He}$ at E = 5.89 GeV

Figure 10: Preliminary results for the spin structure functions g_1 and g_2 on a ^{3}He target for E = 4.73 and 5.89 GeV compared to the world data [14, 19, 37, 38, 45] and the DSSV model [41] and models from Weigel and Gamberg [42], Bourelly and Soffer [43], and Stratmann [44]. (a) and (b): $g_1{}^{3}\mathrm{He}$ and $g_2{}^{3}\mathrm{He}$ for a beam energy of E = 4.73 GeV. (c) and (d): $g_1{}^{3}\mathrm{He}$ and $g_2{}^{3}\mathrm{He}$ for a beam energy of E = 5.89 GeV.

where M is the nucleon mass; α is the electromagnetic fine structure constant; $y = \nu/E$, the fractional energy transfer to the target; θ is the electron scattering angle; σ_0 is the unpolarized total cross section; $A_{\parallel}$ ($A_{\perp}$) is the parallel (perpendicular) double-spin electron asymmetry.

The preliminary results for $g_1{}^{3}\mathrm{He}$ and $g_2{}^{3}\mathrm{He}$ are shown in Figure 10, which compares the data to various models [41, 42, 43, 44] and the world data. Radiative corrections have been applied *only* to the unpolarized total cross sections for the data from this experiment.

References

[1] S. Wandzura and F. Wilczek, Phys. Lett. B **72**, 2 (1977).

[2] R.L. Jaffe, Comm. Nucl. Part. Phys. **19**, 239 (1990).

[3] B.W. Filippone and Xiandong Ji, Adv. Nucl. Phys. **26**, 1 (2001). arXiv:0101224v1 [hep-ph].

[4] M. Burkardt, *The g_2 Spin Structure Function* (2009), arXiv:0905.4079v1 [hep-ph].

[5] M. Burkardt, *Parton Distributions in the Impact Parameter Space* (2008), arXiv:0902.0163v1 [hep-ph].

[6] S. Choi, X. Jiang, Z.-E. Meziani, B. Sawatzky *et al.*, Jefferson Lab PAC E06-014 (2005).

[7] M. Gockeler *et al.*, Phys. Rev. D **72**, 054507 (2005).

[8] P. Solvignon, private communication.

[9] E.V. Shuryak and A.I. Vainshtein, Nucl. Phys. B **201**, 141 (1982).

[10] Ji and Chou, Phys. Rev. D **42**, 3637 (1990).

[11] M. Amerian *et al.*, Phys. Rev. Lett. **89**, 242301 (2002).

[12] K. Slifer *et al.*, *Resonance Spin Structure*, 2008. arXiv:0812.0031.

[13] D. Drechel, S.S. Kamolov and L. Tiatar, Eur. Phys. J. **A34**, 69 (2007).

[14] P.L. Anthony *et al.*, Phys. Lett. B **553**, 18 (2003).

[15] N. Isgur, Phys. Rev. D **59**, 0340123 (1999).

[16] K. Abe *et al.*, SLAC-PUB-7753 (Feb. 1998).

[17] K. Abe *et al.*, Phys. Rev. Lett. **79**, 26 (1997); Phys. Lett. B **405**, 180 (1997).

[18] K. Ackerstaff *et al.*, Phys. Lett. B **404**, 383 (1997).

[19] X. Zheng *et al.*, Phys. Rev. C **70**, 065207 (2004).

[20] E. Leader, A.V. Siderov, D.B. Stamenov, Int. J. Mod. Phys **A13**, 5573 (1998).

[21] J.P. Ralson, P. Jain, R.V. Buniy, AIP Conf. Proc. **549**, 302 (2000).

[22] K.V. Dharmawardane *et al.*, Phys. Lett. B **641**, 11 (2006).

[23] G. Cates, N. Liyanage, Z.-E. Meziani, G. Rosner, B. Wojtsekhowski, X. Zheng *et al.*, Jefferson Lab PAC E1206122 (2006).

[24] G. Cates, J.P. Chen, Z.-E. Meziani, X. Zheng *et al.*, Jefferson Lab PAC E1210101 (2010).

[25] J.L. Friar *et al.*,Phys. Rev. C **42**, 6 (1990).

[26] F. Bissey, A.W. Thomas and I.R. Afnan, Phys. Rev. C **64**, 024004 (2001).

[27] M. Anselmino *et al.*, Phys. Rep. **261**, 1–124 (1995).

[28] D. Parno, Ph.D. Thesis, Carnegie Mellon University (2011).

[29] I. Kominis, Ph.D. Thesis, Princeton University (2001).

[30] J. Singh, *A Note About Beam Depolarization*, Univeristy of Virginia (2008).

[31] M. Posik *et al.*, E06-014 Analysis Status Report 2011, https://hallaweb.jlab.org/wiki/images/8/8c/D2n_HallAReport_2011_v5.pdf

[32] L.W. Mo and Y.S. Tsai, Rev. Mod. Phys. **40**, 205 (1969).

[33] R. Altulmus and J. Wise, rosetail.f, fortran analysis code.

[34] S. Stein *et al.*, Phys. Rev. D **12**, 1884 (1975).

[35] Roy Whitney, radcor.f, fortran analysis code.

[36] P.E. Bosted and V. Mamyan, *Empirical Fit to electron-nucleus scattering* (2012), arXiv:1203.2262v2 [nucl-th].

[37] P.L. Anthony *et al.*, Phys. Rev. D **54**, 6620 (1996).

[38] P. Solvignon *et al.*, Phys. Rev. Lett. **101**, 182502 (2008).

[39] F. Bissey *et al.*, Phys. Rev. C **65**, 064317 (2002).

[40] S.A. Kulagin and W. Melnitchouk, Phys. Rev. C **78**, 065203 (2008).

[41] D. de Florian, R. Sassot, M. Stratmann, W. Vogelsang, *Global Analysis of Helicty Parton Densities and Their Uncertainties*, arXiv:0804.0422 [hep-ph].

[42] H. Weigel, L. Gamberg and H. Reinhart, Phys. Rev. D **55**, 6910 (1997).

[43] C.R.V. Bourrely, J. Soffer and F. Buccella, Eur. Phys. J. C **41**, 327 (2005) [arXiv:hep-ph/0502180].

[44] M. Stratmann, Z. Phys. C **60**, 763 (1993).

[45] K. Kramer *et al.*, Phys. Rev. Lett. **95**, 142002 (2005).